Nanoscale superconducting properties of amorphous W-based deposits grown with a focused-ion-beam

I Guillamón[1], **H Suderow**[1], **S Vieira**[1],
A Fernández-Pacheco[2,3,4], **J Sesé**[2,4], **R Córdoba**[2,4],
J M De Teresa[3,4] **and M R Ibarra**[2,3,4]

[1] Laboratorio de Bajas Temperaturas, Departamento de Física de la Materia Condensada Instituto de Ciencia de Materiales Nicolás Cabrera,
Facultad de Ciencias Universidad Autónoma de Madrid, E-28049 Madrid, Spain
[2] Instituto de Nanociencia de Aragón, Universidad de Zaragoza,
Zaragoza 50009, Spain
[3] Instituto de Ciencia de Materiales de Aragón, Facultad de Ciencias,
Universidad de Zaragoza-CSIC, Zaragoza 50009, Spain
[4] Departamento de Física de la Materia Condensada, Universidad de Zaragoza,
Zaragoza 50009, Spain
E-mail: hermann.suderow@uam.es and deteresa@unizar.es

Abstract. We present very low temperature scanning tunneling microscopy and spectroscopy (STM/S) measurements in W-based amorphous superconducting nanodeposits grown using a metal–organic precursor and a focused-ion-beam. The superconducting gap closely follows s-wave Bardeen–Cooper–Schrieffer theory, and STS images under magnetic fields show a hexagonal vortex lattice whose orientation is related to features observed in the topography through STM. Our results demonstrate that the superconducting properties at the surface of these deposits are very homogeneous, down to atomic scale.

IOP Institute of Physics ⟨Φ⟩ DEUTSCHE PHYSIKALISCHE GESELLSCHAFT

Contents

1. Introduction

Since the seminal work of Buckel [1], which found superconductivity at 7 K in fully amorphous films of Bi (Bi is not superconducting as a crystalline solid at ambient pressure), many materials have been found to deeply change their electrical properties when prepared in an amorphous form [2]. The actual origin of superconductivity, and the relationship to the metal–insulator transition induced by strong disorder, has been the subject of intense debate [3]. However, some of these systems have metallic transport and thermodynamic properties that better approach the free electron model than their crystalline analogs [2]. Moreover, those which are superconducting very often behave as model s-wave Bardeen–Cooper–Schrieffer (BCS) superconductors [2]. This makes them particularly interesting candidates as a reference system where s-wave BCS phenomenology can be probed in newly developed techniques, in particular, in nanoscale tunneling probes of the superconducting state like scanning tunneling microscopy and spectroscopy (STM/S). Many crystalline superconductors, such as high T_c cuprates, MgB_2, heavy fermions, transition metal di-chalcogenides, boron-doped diamond, or nickel borocarbides, have been studied using high resolution STM/S down to the atomic level and in a wide range of temperatures and magnetic fields [4]–[12]. However, an atomic level STM/S experiment over large surfaces in a reference s-wave BCS superconductor is still lacking. In this paper, we report a thorough STM/S study at the atomic scale of amorphous W nanodeposits. We find that the nanodeposits remain fully stable under ambient conditions, showing excellent local tunneling properties. The nanodeposited amorphous system is chemically highly inert, like e.g. $2H–NbSe_2$ or graphite, making this system the long sought paradigm for STM/S studies, with the additional important feature of being easily used for creating nanofabricated superconducting structures.

The W nanodeposits have been grown with a dual-beam system that integrates an electron and an ion column. A major application of this system is the controllable nanodeposition of materials, with widely extended use in nanotechnology and the semiconductor industry for the reparation of lithography masks and integrated circuits [13], the fabrication of three-dimensional nanostructures [14], the creation of electronic nanodevices [15], the protection of sample surfaces for subsequent micromachining for cross-section analysis [16], etc. In the case of ion-beam-induced-deposition (IBID), an ion beam focused to nanometric size (generally based on Ga^+) is swept through the region of interest in a sample, breaking precursor gas molecules previously introduced to the chamber and giving rise to a nanodeposit. The combined use of imaging techniques (secondary-electron or backscattered-electron images) and local growth techniques (IBID) allow precise and flexible deposition in the targeted place, with the lateral

size and deposit thickness being controlled to a large extent. The IBID growth process can be considered a chemical vapor deposition process assisted by an ion beam. The precursor gas molecules containing the material to be deposited flow from a nearby injector towards the substrate and become adsorbed to it. The mechanism proposed to explain the deposition is the collision cascade model where the ions impact on the substrate and transfer energy to surface atoms, which decompose the precursor gas molecules [17]. The role played by the secondary electrons reaching the sample surface has also been highlighted [18]. When the precursor molecules are organic, a carbonaceous matrix is also present, which is relevant for the physical and chemical properties exhibited by the deposit. With the IBID technique, nanodeposits based on metallic materials, such as Au, Pt, W and Cu have been carried out and used in nanotechnological applications [16]–[21]. Amongst the IBID materials, W nanodeposits have been recently found to show superconducting properties [22]–[25].

2. Experimental details

The STM/S measurements were performed on a 200 nm thick film of a W deposit with a lateral size 30 μm × 30 μm grown at the center of a conducting Au layer previously deposited on a Si substrate. The deposit has been made in a similar way to earlier reports [22]–[24], and characterized by means of energy dispersive x-ray microanalysis (EDX), high-resolution transmission electron microscopy (HRTEM), transport measurements and x-ray photoelectron spectroscopy (XPS). The deposit is metallic due to the high content of W (around 40% from EDX), as found previously in nanodeposits of similar composition [22]–[24]. An in-depth study of the chemical composition using XPS and an argon etching process shows that the deposit is very homogeneous, with average concentration W = 40 ± 7%, C = 43 ± 4%, Ga = 10 ± 3% and O = 7 ± 2%. In figure 1, we can see the W 4f spectrum as a function of the sputtering depth. In the inset, a typical fit is shown. The main peak for the W 4f$^{7/2}$ appears at 31.4 eV, associated with metallic W [26, 27]. A minor peak at 32.1 eV, corresponding to tungsten carbide (WC) [26, 27] is also present. A separation of 2.1 eV between the 4f$^{7/2}$ and the 4f$^{5/2}$ components is found in all cases. The ratio between both species across the whole thickness is found to be W/WC = 5.2 ± 0.5. The C 1s spectrum (not shown here) is significantly broad, and can be de-convoluted in three peaks. One at 283.1 eV, due to WC [28, 29], and the others at 284.3 and 285.2 eV, which correspond to amorphous carbon, sp^2 and sp^3 atoms, respectively [28, 29]. The proportion between the two types of carbon (sp^2/sp^3) corresponds to 3.45 ± 0.15 through the profile.

The sample used here was stored for two days under ambient conditions, without any additional surface treatment and then mounted in a low temperature STM thermally anchored to the mixing chamber of a dilution refrigerator. The magnetic field was applied perpendicular to the sample surface. Our setup, described in earlier work, has a very high mechanical stability and we can change *in situ* the scanning window by moving the sample with respect to the tip [11], [30]–[32]. The gold tip was mechanically shaped and then carefully positioned at ambient temperature on top of the nanodeposit. At low temperatures, when approaching the tip to tunneling distance, we immediately found that the tunneling conditions of the nanodeposit were outstanding. The work function always had a high value (several electron volts), and the images and spectra were fully reproducible and independent of the tunneling current (or distance between tip and sample).
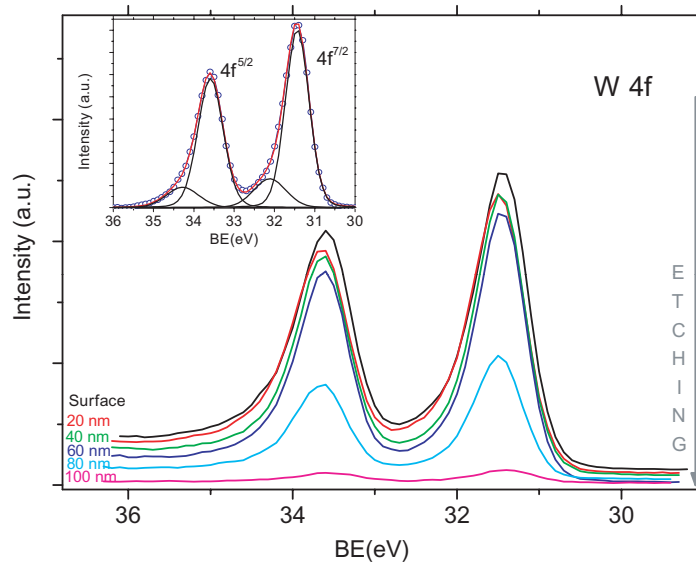
Figure 1. Depth profile spectra of the W 4f core level. Successive spectra are obtained after a 20 nm argon etching process. A typical fit is shown in the inset. The solid lines are the components in which the spectrum is decomposed. The resulting fit is superimposed to the experimental data (open circles). The energies found for the peaks are associated with metallic W and WC (see text). The proportion between the two species (in average W/WC = 5.2(5)) remains approximately constant through all the deposit thickness. For the quantitative analysis of the XPS spectra, we have used pseudo-Voigt peak profiles with a 10–20% Lorentzian contribution, subtracting a Shirley-type background.

3. Results and discussion

Topographic images show that it is possible to scan large areas (figure 2(a)), up to several μm^2, obtaining very uniform scanning profiles. Large regions with surface roughness on the nanometre (nm) range or below and a small inclination (below 5°) appear surrounded by long linear depressions of at most 5–10 nm depth, i.e. between 2 and 5% of the total film thickness (red lines in figure 2(a)). The STM images in the nm range (inset of figure 2(a)) show small groups of randomly distributed atomic size features. The tunneling conductance curve shown in figure 2(b) (taken at 0.1 K) is obtained over whole surface area, without any remarkable changes. The fit to BCS theory is excellent, and gives a value of $\Delta = 0.66$ meV for the superconducting gap, which is slightly higher than the weak coupling BCS value $\Delta_0 = 1.76 k_B T_c = 0.63$ meV($T_c = 4.15$ K). The voltage dependence of the conductance as a function of temperature gives the temperature dependence of the superconducting gap, shown in figure 3, which follows well expectations from BCS theory (solid line in figure 3).

The inset of figure 2(b) shows an STS image constructed from the conductance at the quasiparticle peak in the same region in which the topographic STM image shown in the inset of figure 2(a) was taken. The contrast between black and white corresponds to changes of about 10% of the value of the conductance at the quasiparticle peaks. Corresponding fits to BCS theory show associated changes in Δ below 2%. Clearly, the atomic size features
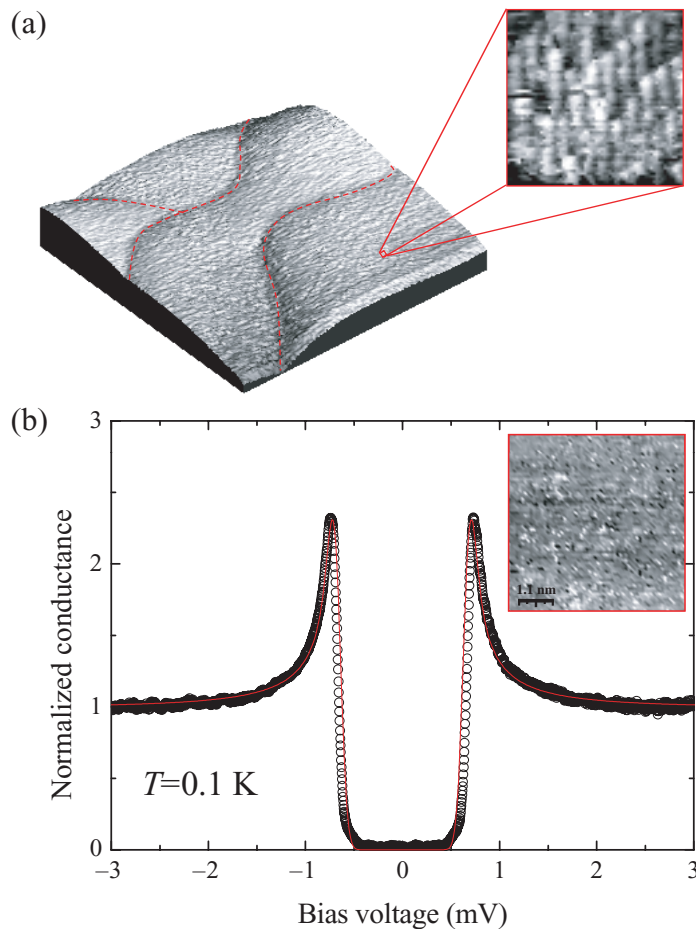
(a)

(b)

Figure 2. A typical topographic STM image is shown in (a) (size $1\,\mu$m $\times\, 1\,\mu$m). Red dashed lines mark the small linear depressions found over the whole surface. Maximum contrast corresponds to height differences of the order of 10 nm, i.e. 5% of the film width. The linear depressions separate atomically flat surfaces. In the inset, we show an atomic size topographic STM image (size 10 nm x 10 nm). In (b), we show the tunneling conductance versus bias voltage typically found over the whole image shown in (a). Red line is a fit to the BCS theory using $\Delta = 0.66$ meV. The inset shows a STS image made in the same area as the inset of (a). The contrast corresponds to changes of about 10% in the tunneling spectra at the voltage position of the quasiparticle peaks.

observed in the topography (STM, inset of figure 2(a)) are not seen in the spectroscopic imaging (STS, inset of figure 2(b)). Similar results are observed when comparing STM and STS images at μm length scale. Therefore, the superconducting density of states $N(E, \mathbf{r})$ can be considered to be homogeneous, in particular if we compare our results to those found in atomic size STS experiments in other kinds of superconducting materials, e.g. the high-T_c cuprate superconductors or 2H–NbSe$_2$. In the cuprate superconductors, periodic modulations of $N(E, \mathbf{r})$ due to surface scattering have provided a great deal of new insight into important properties of the superconducting state, e.g. the anisotropy of the superconducting gap
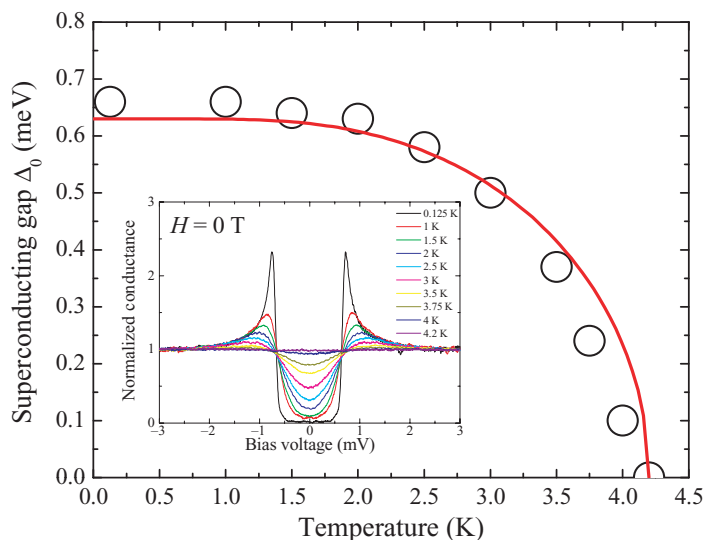
Figure 3. Temperature dependence of the superconducting gap obtained from fits to the tunneling spectra shown in the inset. Red line is the BCS expression, taking $\Delta = 1.76 k_B T_c$ and $T_c = 4.15$ K.

[4]–[6]. In 2H–NbSe$_2$, we could recently demonstrate that the two-band superconducting properties of this compound result in small modulations of $N(E, \mathbf{r})$ that follow lattice periodicity [32]. The absence of any of these effects here demonstrates that the nanodeposit is the first fully isotropic s-wave superconductor that can be studied in detail down to atomic level.

On the other hand, note that the compositional analysis performed with XPS along the full sample thickness (see figure 1) demonstrates that the composition is homogeneous as a function of the depth, up to the surface. This is in clear correspondence with the uniformity of the tunneling characteristics over the whole surface, and demonstrates that the superconducting properties of these deposits have a remarkable overall homogeneity, as may be expected for an amorphous system[5].

When we apply a magnetic field, we observe that, below about 0.2 T, no clear hexagonal vortex lattice is formed in the sample. Vortices appear bunched close to the linear surface depressions observed in the topography (figure 2(a)). Those lying far from the linear depressions, at the smooth and very flat regions surrounded by them, are observed to easily change their position, especially some minutes after changing the field. Above about 0.3 T, however, a clear and very stable vortex lattice is formed. In figure 4, we show some representative examples of STS vortex images obtained from the zero bias conductance changes as a function of the position. The vortex lattice is observed over the full scanning window, and has no long-range order, although, in between the linear depressions in the associated topographic images (marked by red lines in the figure 4), a clear hexagonal Abrikosov lattice is often observed. The right panels of figure 4 are single hexagons obtained far from the linear surface depressions. The intervortex distance d within these hexagons follows conventional

[5] It should be mentioned that previous STM/S experiments in sputtered amorphous TiN films show very inhomogeneous superconducting properties [33].
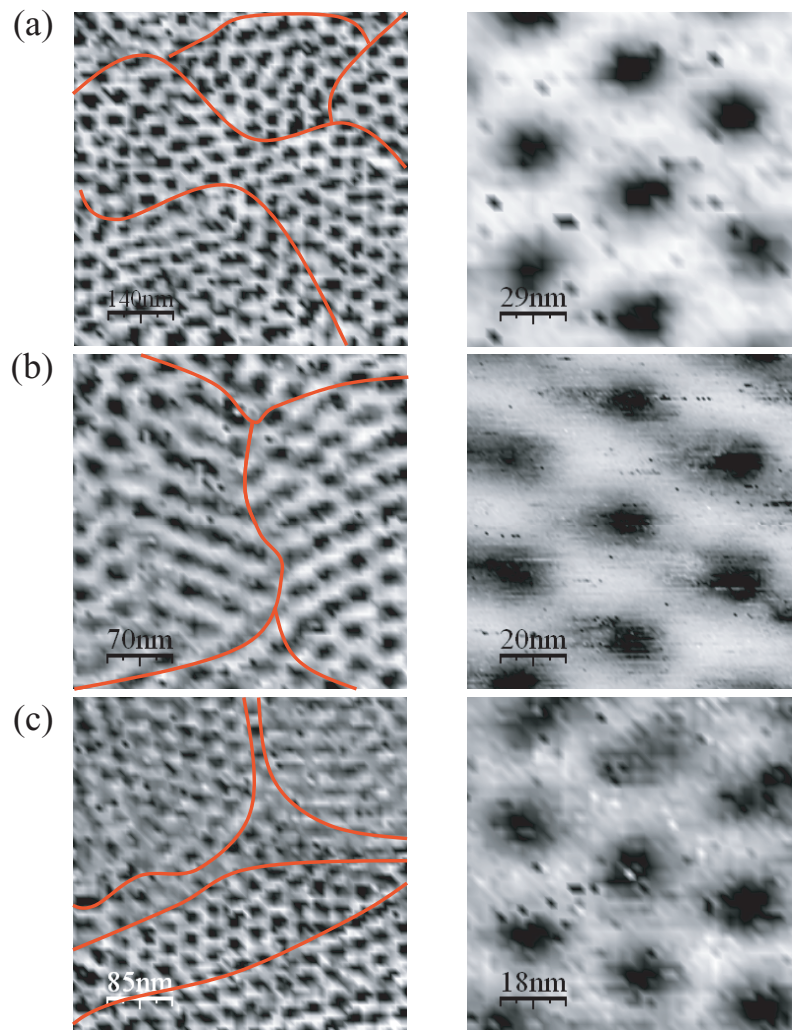
Figure 4. Vortices found at different magnetic fields ((a) at 1 T, (b) at 2 T and (c) at 3 T) obtained from STS images constructed from the Fermi level conductance (shown as raw images, without any filtering or smoothing effects). Left panels show large STS images, and right panels show a single hexagon. The topographic STM images corresponding to the left panels have the small linear surface depressions characteristic of these samples (as discussed in the text and shown in figure 2(a)), along the red lines. The STS images of the right panels are made far from surface depressions, and the corresponding topographic STM images are absolutely flat and featureless, with surface roughness below about 0.5 nm.

expectations for a superconductor with a hexagonal vortex lattice ($d = (1.25)^{1/4}(\frac{\Phi_0}{H})^{1/2}$, where Φ_0 is the flux quantum [34]).

Vortices have a strong tendency to form rows parallel to the linear surface depressions. Correspondingly, the orientation of the hexagons far from the linear depressions slightly changes in different areas. In spite of being very small and smooth changes in the topography of the sample, the surface depressions are clearly the only source of distortion of the Abrikosov

IOP Institute of Physics **ΦDPG** DEUTSCHE PHYSIKALISCHE GESELLSCHAFT

lattice in these samples. Indeed, the pinning properties of transition-metal amorphous systems have been studied thoroughly, and the weak bulk pinning ensures that surface features play a dominant role in the potential landscape that determines the vortex positions [35].

Note that vortices appear sometimes as elongated figures in the images, especially close to the linear depressions. The vortex density in our experiments is high and d is much smaller than the film thickness. So vortex lines can curve in order to hit the surface at a right angle, as the curved length, of the order of d, is small [36]. This effect can easily cause elongated vortex forms in an STS experiment, as e.g. in figure 4(b). Note that this is in sharp contrast to previous vortex imaging experiments in thin films, performed at much smaller magnetic fields using techniques sensitive to the local magnetic field [37, 38]. There, the vortex tilting effects at the surface significantly increase the vortex length and are no longer favorable.

4. Conclusions

In conclusion, we have shown that W IBID grown deposits remain clean after exposure to ambient conditions, have excellent and homogeneous s-wave BCS superconducting properties going up to the surface, and that the vortex configuration is given by the potential landscape formed by small height changes at the surface. Let us put forward that the W IBID technique has great potential for the design of new experiments and devices, with superconducting surface properties which could remain stable to ambient conditions.

Acknowledgments

References

[1] Buckel W and Hilsch R 1956 Superconductivity and electrical resistance in new kinds of tin-bismuth alloys *Z. Phys.* **146** 27
[2] Johnson W L 1981 *Superconductivity in Metallic Glasses. Topics in Applied Physics. Glassy Metals I* ed H J Guntherodt and H Beck (Berlin: Springer)
[3] Lee P A and Ramakrishnan T V 1985 Disordered electronic systems *Rev. Mod. Phys.* **57** 287
[4] Fischer O, Kugler M, Maggio-Aprile I and Berthod C 2007 Scanning tunneling spectroscopy of high-temperature superconductors *Rev. Mod. Phys.* **79** 353
[5] Pan S H, Hudson E W, Lang K M, Eisaki H, Uchida S and Davis J C 2000 Imaging the effects of individual zinc impurity atoms on superconductivity in $Bi_2Sr_2CaCu_2O_{8+\delta}$ *Nature* **403** 746
[6] Gomes K K, Pasupathy A N, Pushp A, Ono S, Ando Y and Yazdani A 2007 Visualizing pair formation on the atomic scale in the high T_c superconductor $Bi_2Sr_2CaCu_2O_{8+\delta}$ *Nature* **447** 569–72
[7] Matsuba K, Yoshizawa S, Mochizuki Y, Mochiku T, Hirata K and Nishida N 2007 Anti-phase modulation of electron- and hole-like states in vortex core of $Bi_2Sr_2CaCu_2O_x$ probed by scanning tunneling spectroscopy *J. Phys. Soc. Japan* **76** 063704

[8] Sacépé B, Chapelier C, Marcenat C, Kacmarcik J, Klein T, Bernard M and Bustarret E 2006 Tunneling spectroscopy and vortex imaging in boron-doped diamond *Phys. Rev. Lett.* **96** 097006

[9] Hess H F, Robinson R B, Dynes R C, Valles J M and Waszczak J V 1989 Scanning-tunneling-microscope observation of the Abrikosov flux lattice and the density of states near and inside a fluxoid *Phys. Rev. Lett.* **62** 214

[10] Rubio-Bollinger G, Suderow H and Vieira S 2001 Tunneling spectroscopy in small grains of superconducting MgB_2 *Phys. Rev. Lett.* **86** 5582

[11] Suderow H, Vieira S, Strand J D, Bud'ko S and Canfield P C 2004 Very-low-temperature tunneling spectroscopy in the heavy-fermion superconductor $PrOs_4Sb_{12}$ *Phys. Rev.* B **69** 060504

[12] Suderow H, Martnez-Samper P, Vieira S, Luchier N, Brison J P and Canfield P C 2001 Tunneling spectroscopy in the magnetic superconductor $TmNi_2B_2C$ *Phys. Rev.* B **64** 020503

[13] Matsui S and Ochiai Y 1996 Focused ion beam applications to solid state devices *Nanotechnology* **7** 247

[14] Puers R and Reyntjens S 2001 Fabrication and testing of custom vacuum encapsulations deposited by focused ion beam direct-write CVD *Sensors Actuators* A **92** 249

[15] De Marco A and Melngailis J 2004 Maskless fabrication of JFETS via focused ion beams *Solid-State Electron.* **48** 1833

[16] Gianuzzi L A and Stevie F A (ed) *Introduction to Focused Ion Beams* (New York: Springer)

[17] Ro J S, Thompson C V and Melngailis J 1994 Mechanism of ion beam induced deposition of gold *J. Vac. Sci. Technol.* B **12** 73

[18] Lipp S *et al* 1996 A comparison of focused ion beam and electron beam induced deposition processes *Microelectron. Reliab.* **36** 1779

[19] Della-Ratta A D, Melngailis J and Thompson C V 1993 Focused-ion beam induced deposition of copper *J. Vac. Sci. Technol.* B **11** 2195

[20] Bannerjee I and Livengood L H 1993 Applications of focused ion beams *J. Electrochem. Soc.* **140** 183

[21] Lin J F, Bird J P, Rotkina L and Bennett P A 2003 Classical and quantum transport in focused-ion-beam-deposited Pt nanointerconnects *Appl. Phys. Lett.* **82** 802

[22] Sadki E S, Ooi S and Hirata K 2004 Focused-ion-beam-induced deposition of superconducting nanowires *Appl. Phys. Lett.* **85** 6206

[23] Sadki E S, Ooi S and Hirata K 2005 Focused ion beam induced deposition of superconducting thin films *Physica* C **426–431** 1547

[24] Luxmoore I J *et al* 2007 Low temperature electrical characterisation of tungsten nano-wires fabricated by electron and ion beam induced chemical vapour deposition *Thin Solid Films* **515** 6791

[25] Spoddig D *et al* 2007 Transport properties and growth parameters of PdC and WC nanowires prepared in a dual-beam microscope *Nanotechnology* **18** 495202

[26] Luthin J and Linsmeier Ch 2000 Carbon films and carbide formation on tungsten *Surf. Sci.* **454–456** 78–82

[27] Xu M, Zhang W, Wu Z and Pu S 2007 Evolution mechanism of nanocrystalline tungsten-carbon and effects *J. Appl. Phys.* **102** 11357

[28] Diaz J, Paolicelli G, Ferrer S and Comin F 1996 Separation of the sp^3 and sp^2 components in the C 1s photoemission spectra of amorphous carbon films *Phys. Rev.* B **54** 8064–9

[29] Haerle R, Riedo E, Pasquarello A and Baldereschi A 2002 sp^2/sp^3 hybridization in amorphous carbon from C 1s core-level shifts: x-ray photoelectron spectroscopy and first-principles calculation *Phys. Rev.* B **65** 045101

[30] Rodrigo J G, Suderow H, Vieira S, Bascones E and Guinea F 2004 Superconducting nanostructures fabricated with the scanning tunnelling microscope *J. Phys.: Condens. Matter* **16** 1151

[31] Crespo M, Suderow H, Bud'ko S, Canfield P C and Vieira S 2006 Local superconducting density of states of $ErNi_2B_2C$ *Phys. Rev. Lett.* **96** 027003

[32] Guillamon I, Suderow H, Guinea F and Vieira S 2008 Intrinsic atomic-scale modulations of the superconducting gap of 2H-$NbSe_2$ *Phys. Rev.* B **77** 134505

[33] Escoffier W, Chapelier C, Hadacek N and Villégier J C 2004 Anomalous proximity effect in an inhomogeneous disordered superconductor *Phys. Rev. Lett.* **93** 217005

[34] Tinkham M 1996 *Introduction to Superconductivity* (Singapore: McGraw International)

[35] Kes P H and Tsuei C C 1983 Two-dimensional collective flux pinning, defects, and structural relaxation in amorphous superconducting films *Phys. Rev.* B **28** 5126

[36] Brandt E H 1993 Tilted and curved vortices in anisotropic superconducting films *Phys. Rev.* B **48** 6699

[37] Plourde B L T, van Harlingen D J, Saha N, Besseling R, Hesselberth M B S and Kes P H 2002 Vortex distributions near surface steps observed by scanning squid microscopy *Phys. Rev.* B **66** 054529

[38] Bending S J 1999 Local magnetic probes of superconductors *Adv. Phys.* **48** 449